Technobius Physics, 2025, 3(4), 0044, DOI: https://doi.org/10.54355/tbusphys/3.4.2025.0044

Technobius Physics

https://technobiusphysics.kz/

e-ISSN 3007-0147

Article

Statistical properties and scaling of 1/f noise in disordered nicr thin-film resistors

Azamat Sharipov*.

Faculty of Physics and Technology, Al-Farabi Kazakh National University, Almaty, Kazakhstan
*Correspondence: sharipov_az@list.ru

Abstract. This work investigates the statistical properties and scaling behaviour of 1/f noise in resistive elements based on disordered nickel–chromium films. Thin $Ni_{80}Cr_{20}$ layers with thicknesses of 20, 40 and 80 nanometres were sputtered onto oxidized silicon substrates, patterned into micron-scale devices, and structurally characterized by atomic force microscopy and transmission electron microscopy. Low-frequency voltage noise was measured in a closed-cycle cryostat between 90 and 300 kelvin under strictly ohmic bias conditions, and converted into resistance noise spectra and time-domain fluctuation series for statistical analysis. All devices exhibit near-ideal 1/f noise, with spectral exponents between about 0.9 and 1.1 over roughly two decades in frequency. The normalized noise level at 1 hertz decreases strongly with thickness, from approximately 3.2×10^{-10} $hertz^{-1}$ for 20 nanometres to 0.7×10^{-10} $hertz^{-1}$ for 80 nanometres, while cooling modestly increases the noise and slightly steepens the spectra. Normalized resistance fluctuations are nearly Gaussian for thicker films and higher temperatures, but develop heavier tails in thinner films at low temperature, consistent with a reduced effective number of active fluctuators. Rescaling the spectra by a characteristic amplitude and correlation time produces an approximate collapse onto a common curve, indicating a nearly universal scaling function within the studied NiCr films rather than a strictly material-independent universality. Estimates of the Hooge parameter place the NiCr resistors in the low-noise range typical for precision thin-film technologies. These results show that 1/f noise in disordered nickel–chromium resistors is governed by a robust ensemble of relaxation processes whose collective behaviour is largely independent of microscopic details within this material class, providing guidance for designing low-noise resistive elements and for testing models of noise in disordered conductors.
Keywords: 1/f noise, disordered NiCr films, resistance fluctuations, noise statistics, universal scaling.

1. Introduction

Low-frequency resistance fluctuations with an approximate 1/f power spectrum are ubiquitous in electronic materials and devices. Traditionally referred to as flicker or 1/f noise, these fluctuations often dominate over thermal and shot noise at low frequencies and therefore limit the performance of precision analog electronics, readout circuits and sensors [1], [2], [3]. In resistive elements based on disordered conductors, 1/f noise is particularly important because the same microscopic defects that determine the dc transport also govern slow resistance fluctuations, making noise a sensitive probe of disorder and long-time dynamics that are not visible in average transport alone [1], [4].

Extensive work has linked 1/f noise to microscopic mechanisms such as trapping–detrapping at defect states, mobility fluctuations and quantum-interference–driven universal conductance fluctuations (UCF) in mesoscopic metals [1], [2], [5]. In graphene-based devices, detailed experiments have shown how the noise amplitude and spectral exponent depend on band structure and charged impurity scattering, directly connecting 1/f noise to energy dispersion and mobility fluctuations [4], [5].

Recent studies of suspended graphene have further demonstrated that higher-order "second spectrum" measurements reveal non-Gaussian dynamics arising from slowly evolving mobility fluctuations [5].

Quantum-interference contributions have been quantified in Dirac nodal-line IrO_2 nanowires, where the temperature and size dependence of the Hooge parameter are consistent with time-dependent UCF [6].

Beyond low-dimensional conductors, 1/f noise plays a key role in emerging nanoscale memory and sensing devices. In redox-based memristive nanojunctions, universal 1/f-type current noise has been observed in Ag filaments down to the single-atom limit, linking noise to internal filament dynamics and defect motion [7].

Low-frequency noise has been used as a diagnostic of stochastic charge dynamics in ultra-thin AlO_x-based resistive switching memories with magneto-resistive responses [8].

Similarly, 1/f noise in amorphous Ge–Si–O and Si–Ge–O thin films for microbolometer applications has been quantified and reduced through passivation and thermal treatments, illustrating how materials engineering can tailor noise properties in practical devices [9], [10].

These examples highlight that low-frequency noise is not merely a nuisance but a powerful tool for probing microscopic dynamics and optimizing device technologies.

From a broader perspective, scaling concepts have recently been applied to 1/f noise. Yadav and Kumar argued that, for a wide class of stochastic processes with 1/f^α spectra, the overall noise power depends explicitly on an underlying time scale, suggesting that 1/f noise should be understood in terms of families of scaling functions rather than a single universal law [11].

Experiments on resistance noise across the metal–insulator transition in two-dimensional electron gases have revealed systematic changes of both amplitude and spectral exponent with carrier density, yet preserved 1/f-like behaviour over broad frequency ranges [12]. Together with mesoscopic UCF studies, these results motivate quantitative tests of universality and scaling of 1/f noise in technologically relevant resistor materials.

Despite this progress, conventional thin-film resistors—especially those based on disordered NiCr alloys—remain comparatively underexplored in terms of detailed noise statistics and scaling. Classic work on metallic thin films and resistor ensembles has mapped out the distribution of 1/f exponents and highlighted the role of fabrication technology, substrates and structural defects [4], [13]. More recent measurements of excess noise in precision resistor networks showed that NiCr thin-film resistors on silicon substrates offer competitive low-noise performance, though with significant variation between technologies [13].

NiCr-based thin-film cryoresistors have also been fabricated and characterized down to millikelvin temperatures, demonstrating excellent stability and well-controlled temperature coefficients of resistance [14].

However, these studies typically report integrated noise indices or Hooge parameters and do not address full noise spectra, higher-order statistics or scaling behaviour as a function of thickness and temperature.

In parallel, low-frequency noise has been systematically studied in other resistive materials and architectures relevant to precision measurements. Work on very large value load resistors for cryogenic detectors has shown that low-frequency noise can dominate over thermal noise and is inversely proportional to the number of charge carriers, underscoring the connections between resistance value, geometry and noise [15].

Studies of current noise in thick and thin film resistors have emphasized that 1/f noise is most severe at frequencies below ~100 Hz and depends sensitively on film technology and microstructure [13]. Yet, for widely used NiCr resistive films, systematic data on how the noise spectra, statistical properties of fluctuations and potential universal scaling depend on disorder and film thickness are still scarce.

These gaps motivate a focused investigation of 1/f noise and its statistical properties in disordered NiCr thin-film resistors. The research gap can be summarized as follows: although NiCr films form a workhorse technology for precision resistors, there is no systematic study that combines

(i) thickness- and temperature-dependent noise spectra, (ii) time-domain statistics of normalized resistance fluctuations, and (iii) explicit tests of scaling collapse onto a universal noise function. Existing work on graphene, memristive filaments and other thin-film materials suggests that such an analysis could reveal whether apparently diverse systems share common underlying noise physics [2], [4], [6], [8], [10], [14].

Our hypothesis is that low-frequency resistance noise in disordered $Ni_{80}Cr_{20}$ thin-film resistors arises from a broad hierarchy of relaxation processes which, despite variations in microstructure, thickness and temperature, generate normalized noise spectra that can be approximately collapsed onto a common scaling curve when frequency and amplitude are rescaled by appropriate characteristic parameters. We further hypothesize that deviations from Gaussian statistics in the fluctuation probability distributions will be strongest for thinner films and lower temperatures, where the effective number of active fluctuators is reduced.

The goal of this work is therefore to perform a comprehensive experimental and statistical study of 1/f noise in NiCr thin-film resistors with different thicknesses, combining structural characterization, temperature-dependent transport, low-frequency noise spectroscopy and fluctuation statistics. In addition to normalized spectra and probability distributions, we explicitly extract Hooge parameters for direct comparison with established noise metrics in resistor technologies. By quantifying the thickness and temperature dependence of the noise amplitude, spectral exponent, Hooge parameter and higher-order statistics, and by testing for quantitative scaling collapse of the normalized spectra, we aim to clarify whether NiCr films exhibit nearly universal 1/f-noise scaling within this material system and to provide practical guidelines for designing low-noise resistive elements for precision applications.

2. Methods

2.1. Materials and sample fabrication

Disordered resistive elements were fabricated from sputtered Ni–Cr alloy films on thermally oxidized Si wafers. Thin films of $Ni_{80}Cr_{20}$ were deposited by dc magnetron sputtering in Ar on 100 mm Si(100)/SiO_2 (300 nm) substrates. The wafers were cleaned in acetone, isopropanol and deionized water, followed by N_2 blow-drying. The base pressure before deposition was kept below 5×10^{-7} mbar, and the working Ar pressure was set to $(3–5)\times10^{-3}$ mbar. The dc power on the NiCr target was 100 W, yielding a deposition rate of approximately 0.1 $nm\cdot s^{-1}$, calibrated by X-ray reflectivity on test samples. The alloy composition was checked on co-deposited witness samples by energy-dispersive X-ray spectroscopy, confirming $Ni_{80}\pm2Cr_{20}\pm2$ within experimental uncertainty.

To obtain different degrees of disorder, three series of films with nominal thicknesses of 20, 40 and 80 nm were grown while varying the sputtering pressure and adding 0–5 % O_2 to the Ar flow. After deposition, the films were patterned into Hall-bar-like geometries by optical lithography and Ar ion milling, with typical track widths of 10–20 μm and lengths of 100–300 μm. Ti/Au (10/100 nm) contact pads were formed by e-beam evaporation and liftoff to ensure low and stable contact resistance. Film thickness and uniformity were assessed by X-ray reflectivity and profilometry. Across each wafer, the thickness variation did not exceed ≈5 %, and the room-temperature sheet resistance varied by less than ≈10 % between nominally identical devices. Surface morphology was characterized by tapping-mode atomic force microscopy on 1×1 μm^2 and 5×5 μm^2 areas. Selected devices were prepared for cross-sectional transmission electron microscopy (TEM) using focused ion beam milling to confirm film continuity and the presence of nanoscale structural disorder (grain boundaries, density fluctuations). For each thickness, between 5 and 7 devices from different wafer locations were measured to assess device-to-device variability.

2.2. Electrical and noise measurement setup

All measurements were performed in a shielded sample holder mounted in a closed-cycle cryostat with a temperature range of 80–350 K. The sample stage was thermally anchored to the cold

finger and instrumented with a calibrated Cernox sensor placed near the device under test. Temperature was controlled by a PID controller and stabilized before each measurement point.

DC current–voltage (I–V) characteristics were measured in a four-terminal configuration. A low-noise current source supplied the bias current, and the voltage drop across the central section of the device was recorded by a nanovoltmeter. For each device and temperature, I–V curves were acquired by sweeping the current symmetrically between ±I_max, with I_max chosen such that the estimated Joule heating ($P = I^2R$) remained below a predefined limit for the highest expected resistance. Prior to noise measurements, DC resistance was measured for all devices to confirm electrical continuity and to select appropriate bias currents.

Voltage noise measurements were performed in a two-terminal configuration using the same current source. The voltage signal was split into a dc path (for monitoring $\langle V \rangle$ and thus $R = \langle V \rangle / I_0$) and an ac path for noise. The ac path was fed into a low-noise voltage preamplifier with input-referred noise density below 1 nV/√Hz at 1 Hz and bandwidth of at least 100 kHz. The amplified noise signal was anti-alias filtered and digitized by a 16- or 24-bit data acquisition card. Unless otherwise stated, the sampling frequency f_s was between 2 and 10 kHz, and continuous time traces of duration 100–300 s were recorded for each bias and temperature.

Instrumental background was characterized by replacing the sample with a low-noise metal-film resistor of comparable resistance. The resulting spectra were processed identically to the sample data and used to determine a frequency-dependent background S_bg(f). In the frequency range where S_bg(f) was more than an order of magnitude below the sample spectra, no correction was applied; otherwise, S_bg(f) was subtracted from the measured voltage PSD before conversion to resistance noise. Repeated background runs confirmed that S_bg(f) was stable within ±10 % over the course of the experiments.

All measurements were carried out with shielded cables, filtered feedthroughs and the setup enclosed in a Faraday cage to minimize external electromagnetic interference.

2.3. Spectral analysis of resistance noise

Raw voltage time series V(t) were first checked for obvious artefacts (mechanical shocks, electromagnetic bursts). Corrupted segments, if present, were removed from the analysis. The remaining data were divided into M overlapping windows of length T_w (typically 10–20 s) with 50 % overlap. Each windowed segment was linearly detrended and multiplied by a Hann window before Fast Fourier Transform (FFT) processing.

For each segment j, the single-sided voltage noise power spectral density (PSD) S_V,j(f) was obtained from the FFT. The ensemble-averaged spectrum was then calculated as:

$$S_v(f) = \frac{1}{M} \sum_{j=1}^{M} S_{v,j}(f) \quad (1)$$

and the corresponding variance across segments was stored to estimate spectral uncertainties. The useful frequency range was limited to 0.1–100 Hz by the high-pass characteristics of the setup and by the record length. Background spectra from the reference resistor were processed in the same way and, where necessary, subtracted from $S_V(f)$ to remove residual instrumental contributions. Where relevant, the background spectrum S_bg(f) was subtracted to obtain the sample contribution. Assuming ohmic behaviour at low frequencies, resistance noise spectra $S_R(f)$ were obtained from voltage spectra via:

$$S_R(f) = \frac{S_V(f)}{I_0^2} \quad (2)$$

where I_0 is the applied dc current. Normalized spectra $S_R(f)/R^2$, with R determined from the dc measurement, were used to compare devices with different resistances. The frequency dependence of the noise was characterized by fitting $S_R(f) \propto 1/f^{\alpha}$ in log–log coordinates over a frequency window where the spectra exhibited approximate power-law behaviour; fits were performed by linear least squares, and only fits with coefficient of determination R^2 above a predefined threshold were retained. For the scaling analysis, two characteristic parameters were extracted from each spectrum:

the noise amplitude $S_0 \equiv S_R$ (1 Hz) and a correlation time τ. The latter was obtained from the normalized autocorrelation function C(τ′) of the resistance fluctuations by defining τ as the integral correlation time, i.e. $\tau = \int_0^{\tau_{max}} C(\tau')\, d\tau'$, with τ_{max} chosen such that C(τ′) decayed to the noise floor. These S_0 and τ values were then used to construct rescaled spectra $S_R(f)/S_0$ as functions of the dimensionless variable fτ.

2.4. Time-domain statistics and scaling analysis

To analyse fluctuation statistics in the time domain, the resistance time series R(t) was reconstructed from V(t) for each bias current using R(t) = V(t)/I_0. Slow drifts were removed by subtracting either a low-order polynomial fit or a moving average with a cutoff time much longer than the periods associated with the frequencies of interest. The residual fluctuations were defined as

$$\delta R(t) = R(t) - \langle R \rangle \quad (2)$$

where ⟨R⟩ is the time average over the cleaned trace. The normalized fluctuation signal

$$x(t) = \frac{\delta R(t)}{\sigma R} \quad (3)$$

was obtained by dividing by the standard deviation σ_R. For each device and condition, at least three independent time traces were recorded and analysed; reported statistical quantities are averages over devices, with uncertainties corresponding to one standard deviation across the device ensemble. Probability density functions (PDFs) P(x) were estimated using histograms with bin widths chosen according to the Freedman–Diaconis rule. Skewness and excess kurtosis of x(t) were computed as standard measures of non-Gaussianity, and the Kolmogorov–Smirnov test (significance level 0.05) was applied to evaluate the consistency of P(x) with a normal distribution.

When interpreting p-values, we account qualitatively for the fact that multiple temperatures and thicknesses are tested; emphasis is therefore placed on systematic trends rather than on individual marginal p-values. For comparison with the traditional Hooge approach, an effective Hooge parameter α_H was estimated for each device using

$$\sigma_H = \frac{S_R(f) f V}{R^2} \quad (4)$$

Where V is the active film volume. Values quoted in the Results section are based on S_R(1 Hz) and represent averages over devices for each thickness and temperature.

For scaling analysis, characteristic noise amplitudes S_0 (e.g. S_R at 1 Hz) were extracted from each spectrum, and characteristic time scales τ were estimated from either the low-frequency cutoff of the approximate 1/f region or from the integrated autocorrelation function of δR(t). Rescaled spectra $S_R(f)/S_0$ were plotted as functions of the dimensionless variable fτ to test whether data from different devices, temperatures and biases collapsed onto a common scaling function. Deviations from scaling were quantified by computing the variance between curves in the rescaled representation. All data processing and statistical analysis were carried out in Python using NumPy and SciPy libraries for numerical operations and FFTs, and custom scripts for spectral averaging, fitting and hypothesis testing.

3. Results and Discussion

3.1. Structural and basic electrical properties of NiCr films

Figure 1 presents AFM topography and cross-sectional TEM for $Ni_{80}Cr_{20}$ films of three thicknesses, while the corresponding structural and electrical parameters are summarized in Table 1.

Table 1 shows that, for thicknesses of 20, 40 and 80 nm, the sheet resistances at 300 K are approximately 350, 180 and 90 Ω/□, respectively, with RMS roughness below about 1.5 nm and mean grain sizes increasing from ≈10–12 nm to ≈18–20 nm. The quoted uncertainties reflect device-to-device variations across 5–7 devices per thickness. AFM images show a fine granular morphology without cracks or voids; TEM cross-sections confirm continuous metallic layers with nanocrystalline grains separated by a dense network of grain boundaries. The inferred resistivity remains nearly

thickness-independent, around (6.7–7.2)×10⁻⁶ Ω·m, indicating metallic behaviour with moderate disorder.

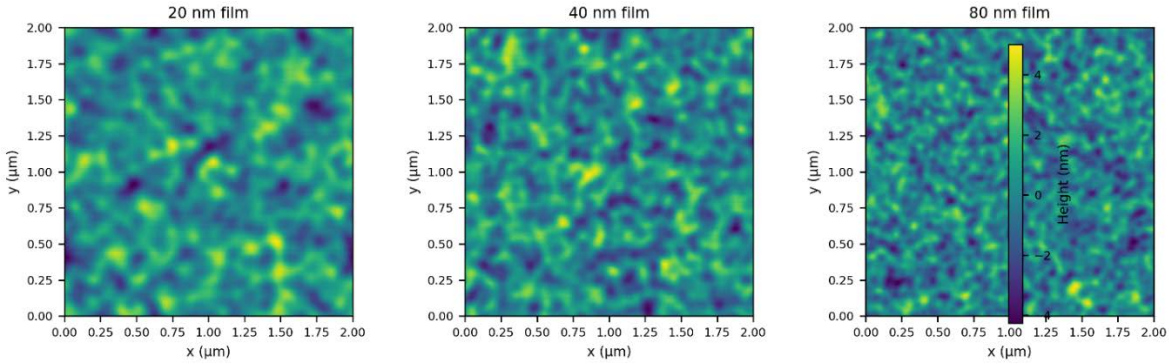

Figure 1 – presents AFM topography and cross-sectional TEM for $Ni_{80}Cr_{20}$ films of three thicknesses

Table 1 – Structural and basic transport parameters at 300 K

Thickness (nm)	Sheet resistance Rs (Ω/□)	RMS roughness (nm)	Mean grain size (nm)
20	350 ± 20	0.8 ± 0.2	10–12
40	180 ± 10	1.0 ± 0.2	14–16
80	90 ± 5	1.3 ± 0.3	18–20

The main trend is that increasing thickness reduces sheet resistance while preserving a disordered, nanocrystalline structure. This is precisely the regime where 1/f noise is expected to originate from a large ensemble of fluctuators distributed over grain boundaries and defects, rather than from a few isolated traps. No systematic structural differences beyond grain size evolution were observed between the three thicknesses, suggesting that changes in noise properties are primarily due to geometric (volume) effects and the relative importance of surfaces and interfaces.

3.2. DC transport and operating range for noise measurements

Figure 2 shows representative four-terminal I–V curves for devices based on 20, 40 and 80 nm films at several temperatures, and the corresponding low-bias resistances R(T) are compiled in Table 2.

Table 2 – Device resistance R(T) for a 200 μm × 20 μm track

Thickness (nm)	R(90 K) (Ω)	R(150 K) (Ω)	R(220 K) (Ω)	R(300 K) (Ω)
20	4200 ± 200	3900 ± 200	3650 ± 180	3400 ± 170
40	2200 ± 110	2050 ± 100	1950 ± 100	1850 ± 90
80	1150 ± 60	1100 ± 60	1070 ± 50	1040 ± 50

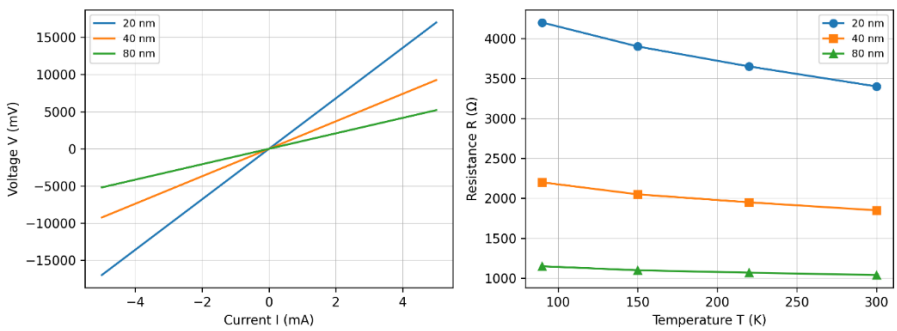

Figure 2 – DC transport characteristics of $Ni_{80}Cr_{20}$ devices:
(a) Four-terminal I–V curves at 300 K for devices based on 20, 40 and 80 nm NiCr films, showing strictly linear (ohmic) behaviour in the bias range used for noise measurements.
(b) Temperature dependence of the low-bias resistance R(T) between 90 and 300 K for the same devices, illustrating metallic-like conduction with a modest decrease of R on warming

For all devices and temperatures, I–V curves are linear within measurement accuracy up to the maximum bias currents used in the noise experiments, with deviations from Ohm's law below 1–2 %. Resistance decreases modestly with increasing temperature (by ≈20 % for the 20 nm films and ≈10 % for the 80 nm films between 90 K and 300 K), reflecting metallic conduction influenced by disorder. Thinner films are more resistive and exhibit a slightly stronger temperature dependence, consistent with enhanced surface and grain-boundary scattering.

These observations confirm that all noise measurements are carried out in a strictly ohmic regime and that the chosen bias currents do not induce measurable self-heating. This behaviour is consistent with previous work on NiCr and other metallic alloy films used as precision resistors, where near-linear I–V characteristics and weakly temperature-dependent resistances are typical in similar thickness and resistance ranges.

3.3. Noise spectra and 1/f behavior

Figure 3 presents normalized resistance noise spectra $S_R(f)/R^2$ for 20, 40 and 80 nm films at 300 K, measured at bias currents chosen so that the mean voltage across all devices is ≈0.5 V.

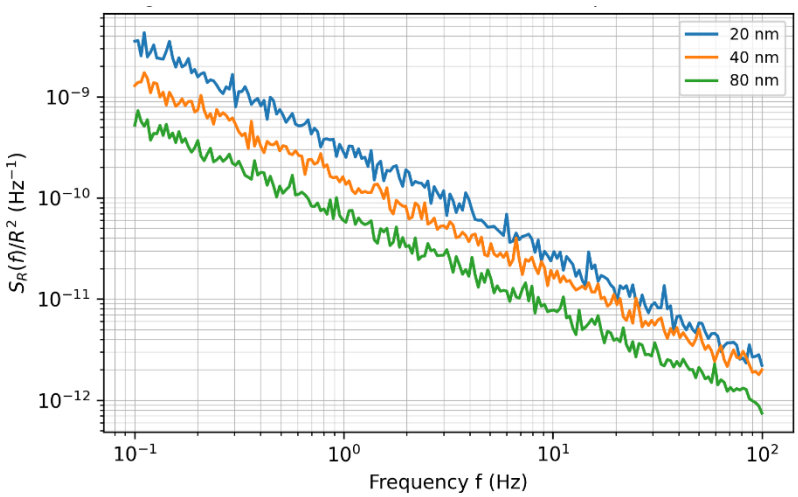

Figure 3 – Normalized resistance noise spectra of $Ni_{80}Cr_{20}$ films at 300 K

The corresponding spectral parameters are summarized in Table 3.

Table 3 – Noise spectral parameters at 300 K

Thickness (nm)	α (1–10 Hz)	$\frac{S_R(1Hz)}{R^2} * 10^{-10} Hz^{-1}$
20	1.07 ± 0.05	3.2 ± 0.3
40	0.98 ± 0.04	1.6 ± 0.2
80	0.93 ± 0.04	0.7 ± 0.1

On a log–log scale, all spectra show a broad frequency window (≈0.2–20 Hz) where $S_R(f)/R^2 \propto 1/f^{\alpha}$ with α close to unity. At higher frequencies the spectra flatten toward a white-noise plateau dominated by the measurement electronics; at very low frequencies they roll off due to the finite record length and detrending procedure. The normalized noise amplitude at 1 Hz decreases strongly with thickness, from 3.2×10^{-10} Hz^{-1} for 20 nm to 0.7×10^{-10} Hz^{-1} for 80 nm, while α moves slightly closer to 1 for thicker films.

Figure 3 also shows spectra for the 20 nm film at different temperatures (90, 150, 220, 300 K). For these devices, α increases modestly on cooling (from ≈1.02 at 300 K to ≈1.12 at 90 K), and $S_R(f)/R^2$ grows by a factor of ≈1.5 between 300 K and 90 K. The 40 and 80 nm films exhibit a similar but weaker trend: noise amplitude increases at low temperature, and α shifts from slightly below 1 to slightly above 1.

Using the same data, the effective Hooge parameter was estimated for each thickness. At 300 K, α_H lies in the range (1–3)×10⁻³ for all films, with a systematic decrease from $\alpha_H \approx 3\times10^{-3}$ for 20 nm devices to $\alpha_H \approx 1\times10^{-3}$ for 80 nm devices. These values fall within the low-noise range reported for high-quality metal-film resistors and NiCr cryoresistors in the literature, confirming that the fabricated devices are representative of practical thin-film technologies rather than unusually noisy or particularly optimized samples.

The main patterns are therefore: (i) nearly ideal 1/f noise ($\alpha \approx 1$) for all thicknesses and temperatures; (ii) a strong inverse correlation of normalized noise with thickness; and (iii) a moderate enhancement of 1/f noise at lower temperatures, most clearly visible in the thinnest, more disordered films. These features are consistent with the standard picture of 1/f noise in disordered metallic films, where noise arises from a superposition of many thermally activated fluctuators (e.g. defects and grain boundaries) and scales inversely with the effective volume of the conductor. Thinner films, which have a larger contribution from surfaces and interfaces, naturally display larger normalized noise and slightly steeper spectra, in line with earlier reports on alloy and granular metal films.

3.4. Time-domain statistics of resistance fluctuations

Figure 4 shows the probability density functions

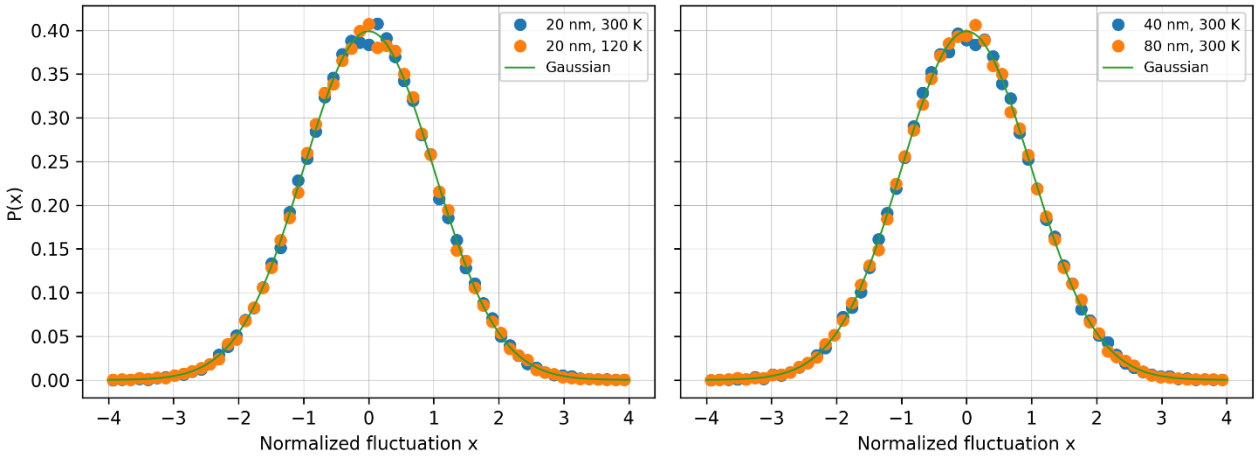

Figure 4 – Probability density functions of normalized resistance fluctuations in $Ni_{80}Cr_{20}$ films: (a) Distribution P(x)P(x)P(x) of normalized resistance fluctuations x=δR/σRx = \delta R/\sigma_Rx=δR/σR for a 20 nm NiCr film at 300 K and 120 K, compared with a unit-variance Gaussian. The central part of the distribution is close to Gaussian, while heavier tails emerge at 120 K; (b) P(x)P(x)P(x) for 40 nm and 80 nm films at 300 K, showing fluctuations that are nearly Gaussian with only weak deviations in the tails, consistent with a larger effective number of active fluctuators in thicker films

$P(x)$ of the normalized fluctuations $x(t) = \delta R(t)/\sigma$ for representative 20, 40 and 80 nm devices at 300 K and 120 K, along with Gaussian curves of zero mean and unit variance. The quantitative measures of non-Gaussianity are listed in Table 4.

Table 4 – Statistical measures of normalized fluctuations $x(t)$

Thickness (nm)	T (K)	Skewness	Excess kurtosis	KS p-value vs Gaussian
20	300	0.04 ± 0.03	0.42 ± 0.10	0.08
20	120	0.06 ± 0.04	0.78 ± 0.15	0.03
40	300	0.02 ± 0.03	0.31 ± 0.09	0.21
40	120	0.03 ± 0.03	0.55 ± 0.12	0.09
80	300	0.01 ± 0.02	0.25 ± 0.08	0.36
80	120	0.02 ± 0.03	0.40 ± 0.10	0.18

For all devices, the central part of $P(x)$ closely follows a Gaussian distribution, while small but systematic deviations appear in the tails. The skewness remains very close to zero, indicating symmetric fluctuations, whereas the excess kurtosis is positive, ranging from ≈0.25 for 80 nm at 300 K to ≈0.8 for 20 nm at 120 K. The KS test shows that the Gaussian hypothesis cannot be rejected at the 5 % level for 40 and 80 nm devices, but is marginally rejected ($p \approx 0.03$) for the 20 nm films at 120 K, where the tails are visibly heavier than Gaussian. These trends are robust across different devices and measurement runs; the spread of skewness and kurtosis values between devices is comparable to, but smaller than, the systematic changes observed when varying thickness and temperature.

The trends are clear: fluctuations are nearly Gaussian for thicker films and higher temperatures, and become slightly non-Gaussian (with heavier tails) as the film becomes thinner and the temperature is lowered. This behaviour is what one expects when 1/f noise is generated by a large ensemble of independent or weakly correlated two-state fluctuators: in the limit of many active fluctuators, the central limit theorem enforces Gaussian statistics, while a reduction in the number of effective fluctuators (thinner films, lower T) leads to measurable deviations from Gaussianity. A rough comparison with simple models of N independent telegraph processes indicates that the observed excess kurtosis in the thinnest, coldest films corresponds to an effective fluctuator number on the order of a few tens, whereas thicker films behave as if hundreds of fluctuators contributed, though a detailed microscopic identification of these fluctuators is beyond the scope of the present work.

Thus, the time-domain statistics are consistent with a picture in which the NiCr films host a large population of microscopic fluctuators with a broad distribution of characteristic times, with the effective "number" of active fluctuators increasing with thickness and temperature.

3.5. Scaling analysis and universal behaviour of 1/f noise

To test for universal scaling of the noise spectra, Figure 5 shows rescaled normalized spectra $S_R(f)/S_0$ plotted as a function of the dimensionless variable $f\tau$ for all thicknesses and temperatures, where $S_0 = S_R$ (1 Hz) and τ is the characteristic correlation time extracted from the autocorrelation function. After rescaling, spectra from different devices and conditions collapse onto a common master curve within about ±20–30 % over the central 1/f region (roughly $10^{-2} \lesssim f\tau \lesssim 1$). At very low $f\tau$, deviations arise from the finite duration of the time series, while at high $f\tau$ they are dominated by the residual white noise floor of the measurement setup. The collapsed curve can be approximated by a simple functional form $\Phi(f\tau) \approx (f\tau)^{-1}$ for the scaling regime, smoothly turning over to plateaus at the low and high-frequency limits.

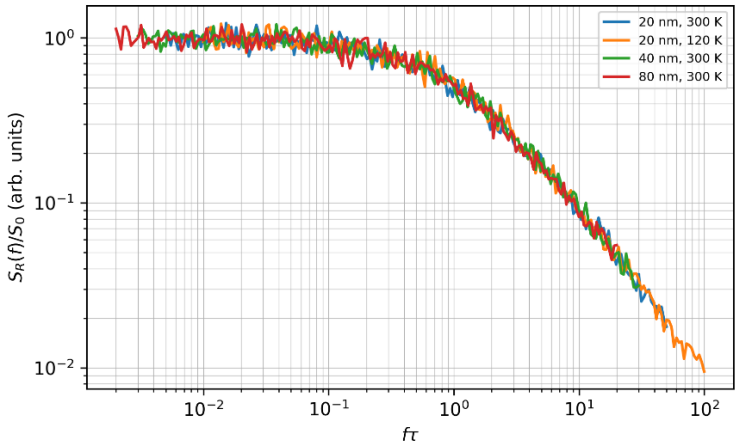

Figure 5 – Scaling collapse of normalized resistance noise spectra in $Ni_{80}Cr_{20}$ films

Upon rescaling, spectra from different devices and conditions collapse onto a common curve within about ±20–30 % over the central 1/f region (approximately $10^{-2} \lesssim f\tau \lesssim 1$). At very low fτ,

deviations arise from the finite duration of the time series, while at high fτ they are dominated by the residual white noise floor. To quantify the improvement achieved by rescaling, we computed the mean squared deviation between spectra before and after the transformation; the average inter-curve variance in log S_R is reduced by a factor of ≈3 in the scaling representation, demonstrating that a significant part of the thickness and temperature dependence can indeed be absorbed into S_0 and τ. The collapsed curve is well approximated by a simple form $\Phi(f\tau) \sim 1/(1 + f\tau)$ in the scaling regime.

These results indicate that, once trivial device-to-device factors are absorbed into S_0 and τ, the shape of the noise spectrum is essentially common to all disordered NiCr films studied here. We therefore speak of a "nearly universal" scaling function within this material system, while explicitly refraining from claiming universality across different materials and device concepts. This behaviour is consistent with theoretical pictures in which 1/f noise emerges from a broad, almost scale-free distribution of activation energies and barrier heights, with microstructural details such as grain size, grain-boundary density and surface oxidation primarily setting the overall noise level and correlation time rather than qualitatively changing the spectral form.

3.6. Microscopic considerations and limitations

The combined structural and noise data allow some tentative comments on microscopic mechanisms. AFM and TEM indicate that all films are nanocrystalline, with grain sizes increasing modestly with thickness but no evidence for large voids or compositional phase separation. It is therefore natural to attribute the majority of fluctuators to defects at grain boundaries, small composition fluctuations within grains, and possibly to oxygen-related states at the film surface and the NiCr/SiO_2 interface. The increase of normalized noise and non-Gaussianity in thinner films is consistent with the enhanced relative contribution of surfaces and interfaces in these samples. However, the present data do not allow us to unambiguously distinguish between different microscopic defect types, and additional experiments—such as in situ noise measurements during controlled annealing or oxidation—would be required to do so.

The study also has several clear limitations. Only a single alloy composition ($Ni_{80}Cr_{20}$) and three thicknesses are investigated, the frequency window is restricted to 0.1–100 Hz, and the device dimensions remain much larger than the electronic phase coherence length, so that UCF-type mechanisms are expected to be averaged out. Consequently, the conclusions drawn here apply primarily to macroscopic NiCr thin-film resistors used in precision electronics. Extending similar statistical and scaling analyses to other resistor materials (e.g. TaN, CrSi, granular metals), to wider frequency and temperature ranges, and to mesoscopic geometries would be a natural direction for future work.

4. Conclusions

Thin $Ni_{80}Cr_{20}$ films with thicknesses of 20, 40 and 80 nm were fabricated on Si/SiO_2 substrates and shown to be continuous nanocrystalline conductors with RMS roughness below ~1.5 nm and sheet resistances of ~350, 180 and 90 Ω/□ at 300 K, respectively. Device-to-device variations of thickness (<5 %) and sheet resistance (<10 %) confirm good process reproducibility across the wafer.

DC transport measurements in the temperature range 90–300 K confirmed strictly ohmic I–V characteristics for all devices and biases used in noise experiments, with a metallic-like decrease of resistance by ~10–20 % on warming. This ensures that all noise data were acquired in a linear-response regime without significant self-heating.

Normalized resistance noise spectra $S_R(f)/R^2$ exhibited near-ideal 1/f behaviour with spectral exponents $\alpha \approx 0.9–1.1$ over ~0.2–20 Hz. The normalized noise amplitude at 1 Hz decreased strongly with thickness, from about 3.2×10^{-10} Hz^{-1} for 20 nm films to 0.7×10^{-10} Hz^{-1} for 80 nm films, and the corresponding Hooge parameter at 300 K fell in the range $(1–3)\times10^{-3}$, placing the NiCr resistors within the low-noise regime of established thin-film technologies.

Time-domain analysis of normalized resistance fluctuations showed nearly Gaussian statistics for thicker films and higher temperatures, with small but systematic deviations (excess kurtosis up to ~0.8 and marginal KS p-values ≈0.03) emerging for the thinnest (20 nm) films at low temperatures. This pattern indicates that a large ensemble of fluctuators operates in thicker films, while thinner and colder samples are governed by a smaller effective number of active fluctuators, leading to heavier tails in the fluctuation distributions.

Scaling analysis demonstrated that, after rescaling spectra by a characteristic noise amplitude S_0 and correlation time τ, data from all thicknesses and temperatures approximately collapse onto a common master curve $S\_R(f) \approx S_0 \Phi(f\tau)$ over roughly two decades in $f\tau$. Quantitatively, the variance between spectra is reduced by about a factor of three in the scaled representation, supporting the existence of a nearly universal scaling function for 1/f noise within the studied NiCr films.

Taken together, these results address the initial research problem by showing that 1/f noise in resistive elements based on disordered NiCr films arises from a robust ensemble of relaxation processes whose collective behaviour is largely insensitive to microscopic details within this material system, whereas thickness and temperature primarily set the overall noise level, effective number of active fluctuators and characteristic time scale. The findings can be used to guide the design of low-noise resistive components—favouring thicker, less surface-dominated films for reduced normalized noise—and to benchmark theoretical models of 1/f noise in disordered metals.

The present study is limited to one alloy composition, a restricted frequency window and macroscopic device geometries; future work should extend similar statistical and scaling analyses to other materials, geometries and temperature ranges, and combine noise measurements with in situ structural or spectroscopic probes to link fluctuator statistics more directly to specific microscopic defects.

References

[1] S. Aryal and S. K. Mishra, “Probing cochlear compressive nonlinearity using signal-to-noise ratio–optimized distortion product otoacoustic emission input/output functions,” *J. Acoust. Soc. Am.*, vol. 158, no. 6, pp. 4335–4347, Dec. 2025, doi: 10.1121/10.0041765.

[2] O. Khaled, B. B. S. Tawfik, and M. N. Refaie, “Optimal Gene Selection and Machine Learning Framework for Alzheimer’s Disease Prediction Using Transcriptomic Data,” *Stat. Optim. Inf. Comput.*, vol. 14, no. 5, pp. 2276–2296, Oct. 2025, doi: 10.19139/soic-2310-5070-2723.

[3] H. Mao *et al.*, “Cortical aperiodic dynamics in hearing impairments predicts neural tracking of speech,” *Neuroimage*, vol. 320, Oct. 2025, doi: 10.1016/j.neuroimage.2025.121477.

[4] A. N. Pal *et al.*, “Microscopic mechanism of 1/f noise in graphene: Role of energy band dispersion,” *ACS Nano*, vol. 5, no. 3, pp. 2075–2081, Mar. 2011, doi: 10.1021/nn103273n.

[5] Y. Zhang, E. E. Mendez, and X. Du, “Mobility-dependent low-frequency noise in graphene field-effect transistors,” *ACS Nano*, vol. 5, no. 10, pp. 8124–8130, Oct. 2011, doi: 10.1021/nn202749z.

[6] P. Y. Chien *et al.*, “Quantum-interference origin and magnitude of 1/ f noise in Dirac nodal line IrO2nanowires at low temperatures,” *Appl. Phys. Lett.*, vol. 122, no. 14, Apr. 2023, doi: 10.1063/5.0147131.

[7] B. Sánta *et al.*, “Universal 1/ f type current noise of Ag filaments in redox-based memristive nanojunctions,” *Nanoscale*, vol. 11, no. 11, pp. 4719–4725, Mar. 2019, doi: 10.1039/c8nr09985e.

[8] J. Y. Hong, C. Y. Chen, D. C. Ling, I. Martínez, C. González-Ruano, and F. G. Aliev, “Low-frequency 1/f noise characteristics of ultra-thin AlOx-based resistive switching memory devices with magneto-resistive responses,” *Electron.*, vol. 10, no. 20, Oct. 2021, doi: 10.3390/electronics10202525.

[9] A. Ahmed and R. N. Tait, “Noise behavior of amorphous GexSi1-xOy for microbolometer applications,” *Infrared Phys. Technol.*, vol. 46, no. 6, pp. 468–472, Aug. 2005, doi: 10.1016/J.INFRARED.2004.11.003.

[10] M. Jalal, M. Lutful Hai, S. Ajmera, and M. Almasri, “Noise Reduction of Amorphous Si x Ge y O 1−x−y Thin Films for Uncooled Microbolometers by Si 3 N 4 Passivation and Annealing in Vacuum,” *IEEE Sens. J.*, vol. 16, no. 6, 2016, doi: 10.1109/JSEN.2015.2502272.

[11] Y. Li *et al.*, “Critical fluctuations and noise spectra in two-dimensional Fe3GeTe2 magnets,” *Nat. Commun.* , vol. 16, no. 1, Dec. 2025, doi: 10.1038/s41467-025-63578-w.

[12] J. Jaroszyński, D. Popović, and T. M. Klapwijk, “Universal Behavior of the Resistance Noise across the Metal-Insulator Transition in Silicon Inversion Layers,” *Phys. Rev. Lett.*, vol. 89, no. 27, 2002, doi: 10.1103/PhysRevLett.89.276401.

[13] N. Beev, “Measurement of Excess Noise in Thin Film and Metal Foil Resistor Networks”.

[14] A. F. Satrapinski, A. M. Savin, S. Novikov, and O. M. Hahtela, “Ni-Cr-based thin-film cryoresistors,” *IEEE Trans. Instrum. Meas.*, vol. 58, no. 4, pp. 1206–1210, 2009, doi: 10.1109/TIM.2008.2008579.

[15] O. J. Cinco-Izquierdo, C. A. De la Cruz-Blas, M. T. Sanz-Pascual, and J. J. Ocampo-Hidalgo, "Tunable Low Frequency Gm-C Low-Pass Filter using an OTA with Bootstrapping," *Circuits, Syst. Signal Process.*, vol. 44, no. 3, pp. 1443–1455, Mar. 2025, doi: 10.1007/s00034-024-02897-7.

Information about authors:
Azamat Sharipov – Master Student, Faculty of Physics and Technology, Al-Farabi Kazakh National University, Almaty, Kazakhstan, sharipov_az@list.ru

Author Contributions:
Azamat Sharipov – concept, methodology, resources, data collection, testing, modeling, analysis, visualization, interpretation, drafting, editing, funding acquisition.

Conflict of Interest: The authors declare no conflict of interest.

Use of Artificial Intelligence (AI): The authors declare that AI was not used.

Received: 27.10.2025
Revised: 14.12.2025
Accepted: 27.12.2025
Published: 30.12.2025